

1
2
3
4
5
6
7
8
9
10
11
12
13
14
15
16
17
18
19
20
21
22
23
24

Revision 3

**Scheelite U-Pb geochronology and trace element geochemistry fingerprint
W mineralization in the giant Zhuxi W deposit, South China**

Word Count: 8928

**Qingqing Zhao¹, Degao Zhai^{1*}, Jingxin Hong¹, Ryan Mathur², Huan Wang³, Han Zhang³,
Yongpeng Ouyang¹, Jiajun Liu¹**

*¹State Key Laboratory of Geological Processes and Mineral Resources, and School of Earth
Sciences and Resources, China University of Geosciences, Beijing, 100083, China*

²Department of Geology, Juniata College, Huntingdon, PA 16652, USA

³Yanduzhongshi Geological Analysis Laboratories Ltd., Beijing, 100094, China

*E-mail: dgzhai@cugb.edu.cn

Revised Submission to: *American Mineralogist*

With 10 Figures and 2 Tables

7-Sep-2022

25

26

ABSTRACT

27

28

29

30

31

32

33

34

35

Skarn-type tungsten deposits are widely distributed all over the world, and contribute more than 70% of the world's W supply. The temporal relation between the W mineralization and causative intrusions, and the evolution of ore-forming fluids are matters of ongoing debate. In this study, we combine in situ LA-ICP-MS U-Pb dating and trace element compositions of scheelite from Zhuxi, the world's largest W deposit, and compare them with literature data to address the above issues. Three primary ore stages exist at Zhuxi: prograde skarn, retrograde skarn and quartz-sulfide stages. Most scheelite occurs in the retrograde skarn stage and is further subdivided into three generations: Sch A, B and C.

36

37

38

39

40

41

42

43

44

45

46

47

48

49

50

51

52

The obtained LA-ICP-MS U-Pb ages for three scheelite generations in the Zhuxi deposit are 154.0 ± 2.8 , 150.3 ± 3.5 and 150.4 ± 6.3 Ma, respectively, indicating that the entire W mineralization is closely related to the emplacement of the nearby Late Jurassic granites (~154 to 150 Ma, zircon U-Pb ages). In situ LA-ICP-MS trace element results demonstrate that Sch A shows the highest Mo content (mean=1002 ppm), where those for Sch B and Sch C are 109 and 45 ppm, respectively. These, combined with the gradually increasing trend of Ce contents and δCe values, indicate a shift from oxidizing to reducing conditions for the ore-forming fluid. All three scheelite generations yield significant positive δEu anomalies, which are considered to be unrelated to the redox state, but caused by the addition of Eu (e.g., feldspar dissolution). The high Y/Ho ratio of scheelite and a good correlation between Y/Ho ratio and δEu ($R^2 = 0.96$) suggest that intense fluid-rock interactions between ore fluids and the Shuangqiaoshan Group metasedimentary rocks as well as earlier-formed skarns drove fluid evolution. This study demonstrates that scheelite U-Pb geochronology is a useful technique when identifying the temporal link between hydrothermal W mineralization and the causative intrusion. The results of this study also highlight that the reactions of the ore fluids with wall rocks and earlier-formed skarns significantly

53 modify the primary fluid compositions.

54 **Keywords:** Scheelite LA-ICP-MS U-Pb dating, trace element, skarn W
55 mineralization, Zhuxi, South China

56 INTRODUCTION

57 Skarn deposits are one of the most abundant ore deposit types in the earth's crust
58 and have been the subject of numerous studies since their discovery (Kwak 1987;
59 Meinert et al. 2005; Romer et al. 2005; Chang et al. 2019). Metal sources for skarn
60 mineralization are critical for establishing robust genetic models for these ore deposits.
61 The close spatial relationship between skarn deposits and plutons indicates a
62 magmatic origin for metals (Audétat et al. 2000; Webster et al. 2004; Thomas et al.
63 2005; Song et al. 2019). In contrast, some others suggest that the metals originated
64 from the surrounding rocks (Linnen and Williams-Jones 1995; Sun et al. 2019).

65 To address this issue, scheelite, which is dominant in skarn-type W deposits
66 (Meinert et al. 2005; Song et al. 2014; Sun et al. 2019), can be adopted as an ideal
67 mineral to constrain the compositions and sources of the fluids and the origins of the
68 metals (Song et al. 2014; Poulin et al. 2018; Choi et al. 2020; Han et al. 2020; Su et al.
69 2021). Scheelite (CaWO_4) commonly accommodates significant amounts of rare earth
70 elements (REE), Y, Mo, and Sr in substitution for Ca or W (Nassau and Loiacono 1963;
71 Ghaderi et al. 1999), which provide insights into the ore-forming processes, including
72 the origin and physicochemical conditions of the ore-forming fluids (Brugger et al.
73 2002; Song et al. 2014; Hazarika et al. 2016; Cao et al. 2021). Meanwhile,
74 developments in U-Pb geochronology permit direct dating of the ore minerals (e.g.,
75 scheelite, cassiterite and wolframite), thus constraining the timing of the mineralizing
76 events (Yuan et al. 2008; Wintzer et al. 2016; Harlaux et al. 2018). Hence, the
77 combination of geochronology and trace element geochemistry of scheelite will shed
78 new light on understanding the genetic relationship between the W mineralization and
79 the causative intrusions. Here, we present in situ laser ablation inductively coupled
80 plasma mass spectrometry (LA-ICP-MS) U-Pb ages and trace element compositions of

81 scheelite from the world's largest skarn-type W deposit to constrain the W
82 mineralization age, reconstruct the redox state of mineralizing fluids, and identify the
83 metal sources.

84 **GEOLOGICAL SETTING**

85 The Zhuxi W deposit is located in Jiangxi Province, South China, within the
86 Jiangnan Orogen, which is adjacent to the Cathaysia block to the south and the
87 Yangtze block to the north (Mao et al. 2017; Fig. 1a, b). The 1500 km long and
88 ENE-trending Jiangnan Orogen was formed by subduction-collision between the
89 Yangtze and Cathaysia blocks at ~970 Ma (Li and McCulloch 1996; Zhang et al.
90 2021). The rocks exposed in this region comprise a Precambrian basement and
91 Phanerozoic rocks (Song et al. 2019; Fig. 1c). The Precambrian basement is
92 subdivided into the lower Shuangqiaoshan Group, which is slate, phyllite and
93 metavolcaniclastic rocks, and the upper Neoproterozoic sedimentary rocks comprising
94 sandstone, slate, conglomerate with lesser carbonate, metabasite and volcanoclastic
95 rocks (Zhao et al. 2011; Zhang et al. 2021). The cover Phanerozoic rocks surrounding
96 the Jiangnan Orogen include Silurian to Early Triassic marine clastic and carbonate
97 rocks, Middle Triassic to Early Jurassic clastic rocks, Middle to Late Jurassic
98 sedimentary and volcanic rocks, and Cretaceous red-bed sandstone, which occur
99 within a series of NE-trending continental basins (Mao et al. 2017, 2020).

100 There are two groups of granites in the Jiangnan Orogen: Neoproterozoic granites
101 that formed during the Jinning orogeny (Li 1999; Wu et al. 2006; Wang et al. 2014)
102 and Late Mesozoic granites that formed during the Yanshanian orogeny (Song et al.
103 2012; Huang and Jiang 2014; Mao et al. 2017; Zhao et al. 2017; Dai et al. 2018). The
104 Yanshanian granitic intrusions can be further subdivided into two groups. The first
105 group (153-136 Ma) consists of monzonitic granite and some granodiorite and alkali
106 granite. The second group (129-102 Ma) is represented by monzonitic granite with
107 peraluminous geochemical signatures (Song et al. 2021).

108 In the past decade, a dozen porphyry-skarn W polymetallic deposits have been

109 discovered in the Jiangnan porphyry-skarn tungsten belt (JNB) in south China (Fig.
110 1c): the Dahutang (1.07 Mt WO₃ at 0.15 wt.%; Mao et al. 2015) and the Dongyuan
111 porphyry deposits (0.14 Mt WO₃ at 0.12 wt.%; Zhou et al. 2011), the Xianglushan
112 (0.22 Mt WO₃ at 0.64 wt.%; Dai et al. 2018) and the Zhuxi skarn deposits (4.22 Mt
113 WO₃ at 0.5 wt.%; Chen et al. 2012, 2015; No. 912 Geological Team 2020).
114 Collectively, these surpass the Nanling W belt (Song et al., 2019), making the JNB the
115 world's largest W belt (up to 6 Mt of WO₃; Mao et al. 2017, 2020). Previous
116 geochronological data revealed that most of the W-bearing deposits in the JNB were
117 related to the first group intrusions (153-135 Ma, e.g., Song et al. 2012; Huang and
118 Jiang 2014; Mao et al. 2017; Pan et al. 2018; Su et al. 2018), while only minor W
119 mineralization was caused by the second group (129-102 Ma, e.g., the Xianglushan
120 skarn deposit, ~125 Ma; Dai et al. 2018).

121 ORE DEPOSIT GEOLOGY

122 The exposed rocks in the Zhuxi deposit include the Neoproterozoic
123 Shuangqiaoshan Group and the Carboniferous-Permian sedimentary rocks (Chen et al.
124 2012). The greenschist-facies Shuangqiaoshan Group mainly consists of slate and
125 phyllite (Wang et al. 2007). It is unconformably overlain by the
126 Carboniferous-Permian rocks, which include the Huanglong, Chuanshan, Changxing,
127 Leping, Maokou and Xixia Formations from older to younger (Yuan et al. 2019; Figs.
128 2a). They mostly comprise shallow marine carbonate rocks (dolomite and limestone)
129 with minor clastic sedimentary rocks (e.g., siltstone, sandstone) (Chen et al. 2012;
130 Sun et al. 2019). These rocks are fractured by NE-trending faults (F1, F2 and F3), and
131 cut by the later NW-trending fault (F4) (Fig. 2a).

132 Detailed core drillings identified three intrusions in the deep part of the deposit:
133 biotite granite, muscovite granite, and granite porphyry (Song et al. 2019; Fig. 2b, c).
134 They occur as dikes and/or stocks intruding into the Neoproterozoic Shuangqiaoshan
135 Group slate and phyllite as well as Carboniferous-Permian carbonates (Chen et al.
136 2012). Recently, Zhang et al. (2021) noted that the granite porphyry caused

137 mineralization. Several lamprophyre dikes in the north of the deposit intruded
138 carbonates (Fig. 2a; Pan et al. 2017), and their zircon U-Pb dating results indicate an
139 emplacement age of ~160 Ma (Liu et al. 2014), which is earlier than the formation
140 age of the Zhuxi deposit.

141 From granites to carbonates, the alteration spatially transforms from greisen, skarn
142 to marble zones (Pan et al. 2018; Yuan et al. 2019). Most W mineralization occurs
143 within the skarn zone (Fig. 3a, b), and minor mineralization also formed in the greisen
144 and marble zones (Fig. 3c) and granites (Yuan et al. 2019; He et al. 2022). The
145 orebodies are stratiform, stratabound or lenticular (Song et al. 2019), and are 750 m
146 long and extend more than 2000 m in depths (Fig. 2b). From the intrusion outwards,
147 the mineralized zones vary from W, W-Cu to Cu-(Pb-Zn) at elevations from -2000 to
148 -200 m (He et al. 2022).

149 The mineralization can be subdivided into three stages: prograde skarn, retrograde
150 skarn, and quartz-sulfide stages; most scheelite was precipitated in the retrograde
151 stage. The prograde stage predominantly consists of anhydrous minerals, such as
152 garnet (Figs. 3d, e and 4a-c), wollastonite (Figs. 3d and 4a), and pyroxene, with minor
153 quartz and vesuvianite (Sun et al. 2019). From core to rim, the skarn veins (several to
154 tens of centimeters in width) exhibit mineral zonation of garnet, pyroxene, vesuvianite
155 and wollastonite, and cut the marble (Pan et al. 2017; Figs. 3d and 4a). This reflects a
156 time sequence with the rim bordering to the carbonates being the oldest one and the
157 axial being the youngest one (Yardley and Lloyd 1995; Heinrich 2007; Xu et al. 2022).
158 Minor scheelite (Sch A) is found in this stage (Figs. 4a-c and 5a) and generally occurs
159 as disseminations in the center of the garnet-wollastonite veins (Fig. 3d) and garnet
160 skarn (Fig. 3e). Most Sch A replaced garnet (Fig. 4b, c) and diopside (Pan et al. 2017)
161 in this stage. The retrograde skarn stage is characterized by the mineral assemblage of
162 abundant tremolite (Fig. 3b), serpentine, muscovite (Figs. 3c and 4d), actinolite,
163 chlorite, fluorite, talc, epidote and quartz (Song et al. 2019). Scheelite (Sch B) in this
164 stage is commonly disseminated (200-1000 μm in diameter) (Figs. 4d, e and 5b), and

165 coexists with quartz, muscovite (Fig. 4d), tremolite and actinolite (He et al. 2022).
166 Notably, coarse-grained massive scheelite (Sch C, up to 0.5 cm in diameter; Figs. 3b,
167 4f, 5c and 5d) is also found in this stage, which may be associated with the dissolution
168 of early disseminated scheelite (Sch A and B) and its re-precipitation at late sequence
169 (Song et al. 2019). Finally, the later quartz-sulfide stage is dominated by the mineral
170 assemblage of chalcopyrite (Fig. 4g, h), sphalerite, molybdenite, bismuthinite, native
171 bismuth (Fig. 4h), pyrrhotite, arsenopyrite, and galena with quartz, fluorite and calcite
172 (Song et al. 2019; Yuan et al. 2019). Both the quartz-sulfide and calcite veins cut the
173 early formed skarns (Figs. 3f and 4i).

174 SAMPLES AND ANALYTICAL METHODS

175 Scheelite samples

176 All the scheelite-bearing specimens were collected from drill core (ZK3001 and
177 ZK3004) along line 30 at depths of -1400 to -1800 m in the Zhuxi deposit (Fig. 2b).
178 These samples were prepared as polished sections for microprobe and LA-ICP-MS
179 analysis. Before analysis, all thin sections were finely polished and coated with
180 carbon, and cathodoluminescence (CL) imaging was carried out in the State Key
181 Laboratory of Geological Processes and Mineral Resources, China University of
182 Geosciences Beijing (CUGB).

183 Major elements analysis

184 Major element compositions of scheelite were determined by electron microprobe
185 analysis using a Shimadzu Electron Probe Microscope Analyzer (EMPA 1720H) at the
186 Key Laboratory of Geoscience Big Data and Deep Resource of Zhejiang Province,
187 Zhejiang University. Operating conditions included an acceleration voltage of 20 kV,
188 a beam current of 20 nA, and an electron beam diameter of 5 μm . Analysis used
189 natural and synthetic minerals as calibration standards, and all data were corrected
190 using a ZAF procedure. The precision of all analyzed elements was better than 1.5%.

191 LA-ICP-MS U-Pb dating and trace element analyses

192 The U-Pb dating of scheelite was performed on an Analytik Jena PlasmaQuant MS

193 quadrupole ICP-MS with a 193 nm NWR193 Ar-F excimer laser at Yanduzhongshi
194 Geological Analysis Laboratories Ltd. Scheelite material ZS-Sch (in-house scheelite
195 standard, 228 ± 2 Ma; [Li et al., 2022](#)) was used as the standard to calibrate the U-Pb age.
196 Instrument drift, mass bias and fractionation of the U-Pb ratio are corrected with a
197 standard-sample bracketing method. Isotopes measured were ^{44}Ca , ^{206}Pb , ^{207}Pb , ^{208}Pb ,
198 ^{232}Th , ^{235}U and ^{238}U . The dwell time was set to 8 ms for ^{44}Ca , 30 ms for ^{206}Pb , 35 ms for
199 ^{207}Pb , 15 ms for ^{208}Pb , 10 ms for ^{232}Th , 15 ms for ^{235}U , 25 ms for ^{238}U .

200 Each analysis on the scheelite began with a 15 second blank gas measurement
201 followed by a further 40 seconds of analysis time when the laser was switched on.
202 Scheelites were sampled on 40-micron spots using the laser at 8 Hz and a density of
203 approximately 4.0 J/cm^2 . A flow of He carrier gas at a rate of 0.6 L/min carried particles
204 ablated by the laser out of the chamber to be mixed with Ar gas and carried to the
205 plasma torch. The raw data were corrected offline employing ICPMSDataCal software
206 ([Liu et al. 2010](#)) and ZSkits software ([Cai et al. 2020](#)). Common Pb was corrected using
207 the ^{207}Pb -based correction method outlined in detail by Chew et al. ([2014](#)). Isoplot 4.15
208 was used to calculate U-Pb ages in the Tera-Wasserburg diagram ([Ludwig 2012](#)), which
209 is particularly useful in systems with high common Pb abundance ([Chew et al. 2011](#),
210 [2014](#)).

211 Trace element measurements of scheelite were separately performed from U-Pb
212 dating using the same instrument conditions. The concentrations of trace elements were
213 quantified using SRM610 as external standard and ^{44}Ca as the internal standard element
214 assuming a stoichiometric scheelite composition.

215 RESULTS

216 Major element compositions

217 The major element compositions of scheelites are listed in [Table 1](#). The WO_3 and
218 CaO contents for scheelites range from 79.9 to 81.3 wt.% and 18.6 to 19.9 wt.%,
219 respectively. The MoO_3 content is up to 0.2 wt.%. In addition to these elements, most
220 other components are negligible and below the detection limit, especially for Nd, Nb

221 and Ta ([Table 1](#)).

222 **LA-ICP-MS trace element compositions**

223 The summarized results of LA-ICP-MS trace element analyses of scheelites are
224 given in [Table 2](#) and detailed data can be found in [Appendix Table A1](#), and the
225 chondrite-normalized REE patterns are shown in [Figure 6](#). Chemically, Sch A contains
226 relatively higher concentrations of Mo (557-1680 ppm) and lower contents of Sr
227 (7.6-16.4 ppm) and rare earth elements (REE; 0.3-11 ppm) compared to Sch B and Sch
228 C ([Table 2](#)). The mean contents of Mo, Sr and REE for Sch B and C are 109, 39, 90 ppm,
229 and 45, 58, 364 ppm, respectively ([Table 2](#)), showing systematically lower Mo contents
230 and increasingly higher Sr and REE from Sch A to Sch C ([Fig. 7a and 7b](#)). The contents
231 of Mn show no significant variation in the three scheelite generations, ranging from 31
232 to 138 ppm, 27 to 74 ppm and 40 to 103 ppm, respectively ([Appendix Table A1](#)).

233 The three generations of scheelite show different chondrite-normalized REE patterns
234 ([Fig. 6a-c](#)). The majority of Sch A are characterized by LREE-enriched patterns, and
235 the LREE/HREE ratios of Sch A vary from 1.9 to 164 with a mean value of 35. The
236 LREE/HREE ratios of Sch B and Sch C, however, are much lower, ranging from 1.7 to
237 8.7 (mean = 4.5) and 2.7 to 6.7 (mean = 4.7), respectively ([Table 2](#)). Notably, almost all
238 of the scheelite spots have positive Eu anomalies and the patterns show depleted MREE
239 relative to LREE and HREE. Among them, some points in Sch C show negative Eu
240 anomalies with significantly higher MREE contents, and the differentiation between
241 LREE and HREE is not obvious ([Fig. 6c](#)).

242 **LA-ICP-MS U-Pb ages**

243 The U-Pb ages obtained in this study are listed in [Appendix Table A2](#) with
244 representative time-resolved depth profiles showing in [Appendix Figure A1](#). For the
245 Sch A (sample 18ZX-15), 22 scheelite grains were analyzed for their U-Pb isotopic
246 ages, which yield an intercept age of 154 ± 2.8 Ma (MSWD = 1.02) ([Fig. 8a](#)). Though
247 the scheelite crystals exhibit relatively high common Pb contents, the corresponding
248 $^{206}\text{Pb}/^{238}\text{U}$ ages after ^{207}Pb -correction range from 141.7 to 165.4 Ma ([Appendix Table](#)

249 A2) with a weighted mean $^{206}\text{Pb}/^{238}\text{U}$ age of 153.7 ± 2.5 Ma ($n = 22$, MSWD = 0.98, 2σ)
250 (Fig. 8b), which is within error of its intercept age (Fig. 8a). Thirty-one scheelite grains
251 (Sch B) (sample 18ZX-21) give an intercept age of 150.2 ± 3.6 Ma (MSWD= 1.8) (Fig.
252 8c) with a weighted mean $^{206}\text{Pb}/^{238}\text{U}$ age after ^{207}Pb -correction of 151.1 ± 2.8 Ma ($n =$
253 31, MSWD = 1.3, 2σ) (Fig. 8d). Finally, 25 spot analyses performed on the
254 coarse-grained scheelite (Sch C) (sample 18ZX-22) from the high-grade W ore yield an
255 intercept age of 150.4 ± 6.3 Ma (MSWD = 0.87) (Fig. 8e) with a weighted mean age of
256 150.7 ± 3.8 Ma ($n = 25$, MSWD = 0.5, 2σ) (Fig. 8f). Because of the low U contents, the
257 age error of Sch C is larger than that of Sch A and Sch B (Appendix Table A2).

258 DISCUSSION

259 Direct time constraint of tungsten mineralization at Zhuxi

260 Numerous studies have been conducted to constrain the mineralization age for the
261 Zhuxi skarn-type W deposit (Liu et al. 2014; Chen et al. 2015). For example, Pan et al.
262 (2017) reported muscovite $^{40}\text{Ar}/^{39}\text{Ar}$ age of 150.2 ± 0.9 Ma. Song et al. (2019) obtained
263 titanite U-Pb ages of 149.9 ± 1.3 to 148.1 ± 7.4 Ma and Zhang et al. (2021) obtained
264 apatite U-Pb ages of 153.7 ± 1.9 to 152.6 ± 4.6 Ma. Recently, Hong et al. (2022)
265 reported garnet U-Pb ages of 153.0 ± 4.4 and 148.7 ± 7.9 Ma. These ages, however, are
266 mostly reported for hydrothermal minerals (i.e., garnet, muscovite, titanite and apatite),
267 which may not temporally coexist with W mineralization and therefore cannot directly
268 represent W mineralization ages.

269 To date, the only geochronology study of the Zhuxi scheelite was conducted by Liu
270 et al. (2017), who reported an age of 144 ± 5 Ma using scheelite Sm-Nd dating method.
271 In addition to the large error of this age, there is an obvious gap between this age and
272 the timing of adjacent granites (recalculated ages of biotite granite, muscovite granite,
273 and granite porphyry are 153.6 ± 0.6 Ma, $n=35$; 150.7 ± 1.2 Ma, $n=28$; and 152.7 ± 0.6
274 Ma, $n=38$; Pan et al. 2018; Zhang et al. 2020). It has been reported that Sm-Nd dating
275 has a high potential to yield rotated mixing lines with too old or too young ages. Thus,
276 the 144 Ma age from scheelite Sm-Nd dating method might be inaccurate. Besides,

277 Pan et al. (2017) reported a molybdenite Re-Os age of 145.1 ± 1.5 Ma. Considering
278 that molybdenite belongs to the sulfide stage and obviously formed later than
279 scheelite, the obtained molybdenite Re-Os age could not represent a primary event for
280 scheelite precipitation. Therefore, the W mineralization age of the Zhuxi deposit
281 requires further investigation.

282 Scheelite has relatively high and variable U concentrations (~ 10 ppm), making it an
283 ideal mineral for U-Pb geochronology (Wintzer et al. 2016; Poitrenaud et al. 2020). The
284 Zhuxi scheelite contains relatively high U contents (6-64 ppm). Time-resolved depth
285 profiles show smooth curves for all the analyzed elements (Appendix Figure A1),
286 ruling out the existence of mineral inclusion and its influence on U-Pb system.
287 Therefore, the U content in scheelite is dominantly structural, and the obtained U-Pb
288 ages can be interpreted as the ages of the tungsten mineralization. There is a negative
289 correction between age error and U content (Appendix Table A2, Fig. 8), indicating that
290 the content of U plays an important role in determining the viability of precise U-Pb
291 dating.

292 Our LA-ICP-MS U-Pb results show that all three scheelite generations (Sch A, Sch B
293 and Sch C) formed between 154.0 ± 2.8 and 150.4 ± 6.3 Ma (Fig. 8), which is
294 consistent with the ages of other hydrothermal minerals in the Zhuxi W deposit (e.g.,
295 muscovite, titanite and apatite; Pan et al. 2017; Song et al. 2019; Zhang et al. 2021) and
296 adjacent granites (recalculated zircon U-Pb ages from 153.6 ± 0.6 to 150.7 ± 1.2 Ma;
297 Pan et al. 2018; Zhang et al. 2020). Compared to scheelite Sm-Nd age (144 ± 5 Ma; Liu
298 et al. 2017), the obtained ages of Sch A to C (154-150 Ma) are more consistent with
299 those of adjacent granites (153.6-150.7 Ma). Overall, the Zhuxi granite, garnet, apatite,
300 muscovite and scheelite were formed almost contemporaneously from 154 to 150 Ma.
301 The consistency of these ages supports the reliability of the scheelite U-Pb dating in
302 identifying W mineralization. The results from this study also show that the Zhuxi
303 tungsten mineralization is closely related to the Late Jurassic to Early Cretaceous
304 magmatism.

305 **Element substitution mechanism in scheelite**

306 The contents of Sr, Mn, and Pb of scheelite in Zhuxi are relatively high,
307 indicating these divalent cations could directly enter the scheelite lattice to replace Ca^{2+}
308 due to the similar ionic radius (Nassau and Loiacono 1963; Ghaderi et al. 1999; Ding et
309 al. 2018). As to REE^{3+} , several charge-compensating mechanisms have been proposed
310 to maintain the charge-compensating to maintain electrostatic neutrality (Cottrant 1981;
311 Burt 1989; Ghaderi et al. 1999; Zhao et al. 2018). The very low concentrations of Na
312 and Nb in Zhuxi scheelite (Tables 1 and 2) and the poor correlation between Nb and
313 REE-Eu+Y (Fig. 7c) indicate that the mechanisms ($2\text{Ca}^{2+} = \text{REE}^{3+} + \text{Na}^+$ and $\text{Ca}^{2+} +$
314 $\text{W}^{6+} = \text{REE}^{3+} + \text{Nb}^{5+}$) are insignificant for the REE accommodation. Furthermore, there
315 is no linear relationship between Nb and Mo (Fig. 7d), which excludes the possibility of
316 the substitution: $\text{Ca}^{2+} + \text{Mo}^{6+} = \text{REE}^{3+} + (1 - x) \text{Mo}^{5+} + x\text{Nb}^{5+}$ ($0 \leq x \leq 1$) (Zhao et al.
317 2018). Previous studies also revealed that scheelite with $\text{REE}^{3+} + \text{Na}^+$ substitution
318 mechanism has obvious MREE-rich (hump-shaped) patterns (Ding et al. 2018), which
319 is not observed in the Zhuxi scheelite (Fig. 6).

320 The REE in skarn minerals are the combination of the REE present in the
321 carbonates and the REE added by the fluid. As the REE are relatively immobile in most
322 fluids (depending on the ligands available), the REE are commonly less abundant for
323 incorporation. In the Zhuxi deposit, because the low contents of Na and Nb, the above
324 substitution mechanisms are excluded. As a result, scheelite accommodates low
325 concentrations of the REE, therefore there is little fractionation between fluid and
326 scheelite. Overall, excluding the other three possibilities, the mechanism $3\text{Ca}^{2+} =$
327 $2\text{REE}^{3+} + [\]\text{Ca}$ (where $[\]\text{Ca}$ represents a Ca-site vacancy; Ding et al. 2018) best
328 explains the REE substitution in scheelite in the studied deposit.

329 **Redox conditions during W mineralization**

330 In the Zhuxi deposit, scheelite from all three generations show predominantly high
331 $\text{Eu}_N/\text{Eu}^*_N$ ratios (δEu) (Fig. 9a) and significant positive Eu anomalies ($\delta\text{Eu} > 1$; Fig. 9b
332 and 9c). Because Eu^{2+} has the same charge as Ca^{2+} , Eu can substitute for Ca in scheelite

333 easily in reducing conditions, which could result in a positive Eu anomaly (Sun and
334 Chen 2017; Poulin et al. 2018; Han et al. 2020). Similarly, Mo can occur in Mo⁶⁺ and
335 Mo⁴⁺ states, and the former can easily substitute for W⁶⁺ whereas the latter hardly
336 substitutes for W⁶⁺, leading to the high Mo contents in oxidizing conditions and low
337 contents in reducing conditions (Yuan et al. 2019). Song et al. (2014) reported a
338 negative correlation between Mo and Eu_N/Eu*_N in porphyry-skarn deposits. However,
339 there is a significant decoupling relationship between Mo content and Eu_N/Eu*_N in the
340 Zhuxi deposit. From Sch A to Sch C, the Mo content decreases but there is no
341 accompanying change in Eu_N/Eu*_N ratio (Fig. 9b). In addition to the redox state, the
342 crystallization of early minerals may have an effect on Mo distribution in scheelite. For
343 instance, the early crystallization of garnet may favor partition of Mo, Sn, and W into
344 this mineral phase (Xu et al., 2016; Fei et al., 2019; Zhu et al., 2021), thus the coeval
345 scheelite will have relatively low contents of these elements, as their source has been
346 depleted. However, previous studies have shown that the Zhuxi garnets contain
347 extremely low contents of Mo (<1ppm; Ouyang et al, 2020). By contrast, the coeval
348 scheelites (Sch A) yield relatively high contents of Mo (up to 1680 ppm), ruling out the
349 possibility of the influence from mineral crystallization. Therefore, the variation of Mo
350 content suggests that the fluid changes from oxidizing to reducing conditions during
351 mineralization.

352 In addition to Eu and Mo, Ce can also be adopted to trace redox conditions (Ding et
353 al. 2015). Because Ce³⁺ (radius of 1.14 Å) is easier to enter scheelite (Ca²⁺ radius of
354 1.12 Å) than Ce⁴⁺ (radius of 0.97 Å), scheelite formed by the oxidizing fluid will
355 contain a low Ce content with negative Ce anomaly. This can be recorded from the Mo
356 vs. Ce and Mo vs. δCe plots (Fig. 9d and 9e), on which Ce contents and δCe decrease
357 with increasing Mo contents in the Zhuxi deposit. The Sch A has the highest Mo
358 contents and lowest Ce contents with significantly negative δCe values (0.5-1.2, mean
359 = 0.8), suggesting an oxidized condition. The δCe values of Sch B (0.8-1.0, mean = 0.9)
360 and Sch C (1.0-1.3, mean = 1.0) indicate that the fluid shifted from oxidation to

361 reduction (Fig. 9e), and are consistent with the variations of Mo contents. The Mo, Ce
362 and δCe variations in scheelite show that the ore fluid has undergone a transition from
363 oxidizing to more reducing conditions. However, there is no significant difference in
364 δEu values of the three scheelite generations (Fig. 9f), which may be caused by Eu^{2+}
365 addition into the fluids (Yuan et al. 2019), partly due to the plagioclase dissolution.

366 In recent years, several studies have also found that there are limitations in using δEu
367 to constrain redox state not only in skarn deposits but also in porphyry-related and/or
368 orogenic deposits. For example, all types of scheelite in the Nui Phao W deposit from
369 Vietnam are characterized by negative Eu anomalies (Nguyen et al. 2020), suggesting
370 that it is necessary to consider the effects of fluid compositions and mineral
371 crystallization. Sciuba et al. (2020) noted that strong positive Eu anomalies are
372 predominantly related to flat REE patterns with low REE contents in scheelite, whereas
373 weakly positive to negative Eu anomalies are characteristic of scheelite with higher
374 REE contents in orogenic deposits. Europium anomalies likely reflect initial fluid
375 $\text{Eu}^{2+}/\text{Eu}^{3+}$ ratios, redox state, temperature, as well as the Na activity during
376 crystallization (Ghaderi et al. 1999; Sciuba et al. 2020). Therefore, it is difficult to
377 define the redox state by δEu alone, and it is necessary to make a comprehensive
378 consideration to judge the evolution history of fluid and its redox state variation for
379 different kinds of ore deposits.

380 **Reaction between fluid and rock during fluid evolution**

381 As stated above, the consistent ages of scheelite and granitic intrusions (ca. 154-150
382 Ma) suggest that the Zhuxi W mineralization is closely related to the intrusions. All the
383 Zhuxi scheelites demonstrate an obvious positive correlation between Y and Ho
384 contents (Fig. 10a), which are consistent with previously obtained data (Fig. 10b; Yuan
385 et al. 2019; Sun et al. 2019). However, these ratios of scheelite are significantly higher
386 than the chondrite Y/Ho ratio of 28, and also higher than those of the related intrusions
387 (from 16 to 42, mean = 23; Pan et al. 2018; Zhang et al. 2020) and the Shuangqiaoshan
388 Group slate (from 20 to 39, mean = 29; Zhang et al. 2012).

389 It has been suggested that, due to the similar ionic radii and ionic charge, Y and Ho
390 display a similar geochemical behavior during various geological processes with a
391 consistent chondritic Y/Ho ratio of 28 for most igneous rocks and clastic sediments
392 (Bau 1996; Ding et al. 2018). However, previous studies have also shown that the Y/Ho
393 ratio in scheelite can be affected by fluid mixing (Liu et al. 2019) or Y-(Ho)-rich
394 minerals precipitation (e.g., garnet is a Y-enriched mineral, the Y/Ho ratio of fluid will
395 decrease after garnet precipitation; Ding et al. 2018). Therefore, though it may be
396 difficult to distinguish fluid sources using Y/Ho ratios, significantly different ratios
397 could be useful tracers of the evolution of ore-forming fluid (Bau 1996; Sun et al.
398 2019).

399 The Sch A is characterized by low REE contents, indicating a REE-depleted fluid,
400 which may be caused by the crystallization of REE-rich minerals (e.g., apatite, up to
401 1000 ppm REE; Song et al., 2021). Meanwhile, we consider that the high Y/Ho ratios
402 in Sch A most likely originate from Y released from garnet instead of the residual fluid
403 after garnet crystallization, as the Sch A usually coexists and replaces the early-formed
404 garnet. The REE are not highly enriched in garnet, so this mineral could not have singly
405 provided the REE in Sch A, the excess Y produced by its dissolution can still increase
406 the Y/Ho ratio of the REE-depleted fluids.

407 Moreover, there is a very good correlation ($R^2 = 0.96$, $n = 20$) between the Y/Ho ratio
408 and δEu value of the coarse-grained Sch C (Fig. 10b). The core of the scheelite (with
409 dark CL image; Figs. 5c and 10b) contains extremely high Y/Ho ratio (up to 213) and
410 δEu value (up to 36.2), which may be caused by the dissolution of garnet and
411 plagioclase. The Y/Ho ratio gradually decreases from core to rim, to values close to
412 those of granite and Shuangqiaoshan Group metasedimentary rocks (Fig. 10b),
413 consistent with intense fluid-rock interactions. The Sch C is characterized by high Sr
414 contents (mean = 58 ppm), which are higher than those of adjacent granites (mean = 6
415 ppm, Zhang et al. 2020). In contrast, a previous study noted that the Shuangqiaoshan
416 Group metasedimentary rocks have high Sr contents (mean = 120, Zhang et al. 2012).

417 Thus, the linear relationship between the Y/Ho ratio and δEu for Sch C is plausibly
418 explained by reaction between the ore-forming fluid and the Shuangqiaoshan Group
419 rocks. Overall, the ore-forming fluid exsolved from magma has experienced intense
420 interactions with surrounding rocks and/or earlier-formed skarns (e.g., garnet), leading
421 to distinctive variations in the trace element composition of these fluids.

422

423

IMPLICATIONS

424 This study presents U-Pb ages and trace element data of scheelite with the aim to
425 constrain the mineralizing event and fluid evolution for a skarn ore system. We firstly
426 report scheelite U-Pb data from the world's largest skarn W deposit at Zhuxi, which
427 yield mineralizing ages from 154.0 ± 2.8 to 150.4 ± 6.3 Ma. These results are consistent
428 with the age of adjacent granite and thus support a close genetic relationship between
429 W mineralization and granitic magmatism. We highlight that scheelite LA-ICP-MS
430 U-Pb dating is a useful technique to determine the mineralization age of a skarn-type W
431 deposit, which will be also useful for understanding the timing of various types of
432 mineralization associated with scheelite formation.

433 The relationships among Y/Ho ratios and metal contents of granite, scheelite and
434 garnet at Zhuxi indicate that the reaction between ore fluids and early-formed garnet
435 could lead to a high Y/Ho ratio for the evolved ore-forming fluid, and the lower Y/Ho
436 ratios and δEu values could be caused by the reaction between ore-forming fluid and
437 the Shuangqiaoshan Group rocks. Therefore, the results from this study contribute to a
438 better understanding of the fluid evolution for the skarn-type ore deposits using Y/Ho
439 ratios.

440

441

ACKNOWLEDGMENTS AND FUNDING

442 This research was supported financially by the National Natural Science Foundation
443 of China (Grants 42122012, 41973038), and the 111 Project of the Ministry of Science
444 and Technology (BP0719021). Constructive suggestions from Constantinos

445 Mavrogonatos and an anonymous reviewer, and the helpful suggestions from the
446 Associate Editor Paul Tomascak and Editor-in-Chief Hongwu Xu significantly
447 improved this manuscript.

448

449

REFERENCES CITED

450 Audétat, A., Günther, D., and Heinrich, C.A. (2000) Magmatic-hydrothermal evolution
451 in a fractionating granite: A microchemical study of the Sn-W-F-mineralized Mole
452 Granite (Australia). *Geochimica et Cosmochimica Acta*, 64, 3373–3393.

453 Bau, M. (1996) Controls on the fractionation of isovalent trace elements in magmatic
454 and aqueous systems: Evidence from Y/Ho, Zr/Hf, and lanthanide tetrad effect.
455 *Contributions to Mineralogy and Petrology*, 123, 323–333.

456 Brugger, J., Maas, R., Lahaye, Y., Mcrae, C., Ghaderi, M., Costa, S., Lambert, D.,
457 Bateman, R., and Prince, K. (2002) Origins of Nd-Sr-Pb isotopic variations in
458 single scheelite grains from Archaean gold deposits, Western Australia. *Chemical*
459 *Geology*, 182, 203–225.

460 Burt, D.M. (1989) Compositional and phase relations among rare earth elements.
461 *Reviews in Mineralogy*, 21, 259–307.

462 Cai, P.R., Wang, T., Wang, Z.Q., Li, L.M., Jia, J.L., and Wang, M.Q. (2020)
463 Geochronology and geochemistry of late Paleozoic volcanic rocks from eastern
464 Inner Mongolia, NE China: Implications for igneous petrogenesis, tectonic setting,
465 and geodynamic evolution of the south-eastern Central Asian Orogenic Belt.
466 *Lithos*, 362–363, 105480.

467 Cao, J.Y., Li, H., Algeo, T.J., Yang, L., and Tamehe, S. (2021) Two-stage magmatism
468 and tungsten mineralization in the Nanling Range, South China: Evidence from
469 the Jurassic Helukou deposit. *American Mineralogist*, 106, 1488–1502.

470 Chang, Z.S., Shu, Q.H., and Meinert, L. (2019) Skarn deposits of China. In: Chang,
471 Zhaoshan, and Goldfard, Richard J., (eds.) *Mineral Deposits of China*. Special
472 Publications of the Society of Economic Geologists, 22. Society of Economic

- 473 Geologists, Littleton, CO, USA, pp. 189–234.
- 474 Chen, G.H., Wan, H.Z., Shu, L.S., Zhang, C., and Kang, C. (2012) An analysis on ore
475 controlling conditions and geological features of the Cu-W polymetallic ore
476 deposit in the Zhuxi area of Jingdezhen, Jiangxi Province. *Acta Petrologica Sinica*,
477 28, 3901–3914 (in Chinese with English abstract).
- 478 Chen, G.H., Shu, L.S., Shu, L.M., Zhang, C., and Ouyang, Y.P. (2015) Geological
479 characteristics and mineralization setting of the Zhuxi tungsten (copper)
480 polymetallic deposit in the Eastern Jiangnan Orogen. *Science China Earth
481 Sciences*, 45, 1799–1818 (in Chinese with English abstract).
- 482 Chew, D.M., Sylvester, P.J., and Tubrett, M.N. (2011) U-Pb and Th-Pb dating of apatite
483 by LA-ICPMS. *Chemical Geology*, 280, 200–216.
- 484 Chew, D.M., Petrus, J.A., and Kamber, B.S. (2014) U-Pb LA-ICPMS dating using
485 accessory mineral standards with variable common Pb. *Chemical Geology*, 363,
486 185–199.
- 487 Choi, W., Park, C., and Song, Y. (2020) Multistage W-mineralization and magmatic
488 hydrothermal fluid evolution: Microtextural and geochemical footprints in
489 scheelite from the Weondong W-skarn deposit, South Korea. *Ore Geology
490 Reviews*, 116, 103219.
- 491 Cottrant, J.F. (1981) *Cristallochimie et géochimie des terres rares dans la scheelite:*
492 *Application à quelques gisements français.* Ph.D. thesis, University of Paris-VI,
493 France.
- 494 Dai, P., Mao, J.W., Wu, S.H., Xie, G.Q., and Luo, X.H. (2018) Multiple dating and
495 tectonic setting of the Early Cretaceous Xianglushan W deposit, Jiangxi Province,
496 South China. *Ore Geology Reviews*, 95, 1161–1178.
- 497 Ding, T., Ma, D.S., Lu, J.J., and Zhang, R.Q. (2015) Apatite in granitoids related to
498 polymetallic mineral deposits in southeastern Hunan Province, Shi-Hang zone,
499 China: Implications for petrogenesis and metallogenesis. *Ore Geology Reviews*,
500 69, 104–117.

- 501 Ding, T., Ma, D., Lu, J., and Zhang, R. (2018) Garnet and scheelite as indicators of
502 multi-stage tungsten mineralization in the Huangshaping deposit, southern Hunan
503 province, China. *Ore Geology Reviews*, 94, 193–211.
- 504 Fei, X.H., Zhang, Z.C., Cheng, Z.G., and Santosh, M. (2019) Factors controlling the
505 crystal morphology and chemistry of garnet in skarn deposits: A case study from
506 the Cuihongshan polymetallic deposit, Lesser Xing'an Range, NE China.
507 *American Mineralogist*, 104, 1455–1468.
- 508 Ghaderi, M., Palin, J.M., Campbell, I.H., and Sylvester, P.J. (1999) Rare earth element
509 systematics in scheelite from hydrothermal gold deposits in the
510 Kalgoorlie-Norseman region, Western Australia. *Economic Geology*, 94, 423–
511 437.
- 512 Han, J.S., Chen, H.Y., Hong, W., Hollings, P., Chu, G.B., Zhang, L., and Sun, S.Q.
513 (2020) Texture and geochemistry of multi-stage hydrothermal scheelite in the
514 Tongshankou porphyry-skarn Cu-Mo(-W) deposit, eastern China: Implications for
515 ore-forming process and fluid metasomatism. *American Mineralogist*, 105, 945–
516 954.
- 517 Harlaux, M., Romer, R.L., Mercadier, J., Morlot, C., Marignac, C., and Cuney, M.
518 (2018) 40 Ma of hydrothermal W mineralization during the Variscan orogenic
519 evolution of the French Massif Central revealed by U/Pb dating of wolframite.
520 *Mineralium Deposita*, 53, 21–51.
- 521 Hazarika, P., Mishra, B., and Pruseth, K.L. (2016) scheelite, apatite, calcite and
522 tourmaline compositions from the late Archean Huttu orogenic gold deposit:
523 Implications for analogous two stage ore fluids. *Ore Geology Reviews*, 72, 989–
524 1003.
- 525 He, X.L., Zhang, D., Di, Y.J., Wu, G.G., Hu, B.J., Huo, H.L., Li, N., and Li, F. (2022)
526 Evolution of the magmatic-hydrothermal system and formation of the giant Zhuxi
527 W-Cu deposit in South China. *Geoscience Frontiers*, 13, 101278.
- 528 Heinrich, W. (2007) Fluid immiscibility in metamorphic rocks. In: Liebscher, A.,

- 529 Heinrich, C.A. (Eds.), Fluid–Fluid Interactions, Reviews in Mineralogy and
530 Geochemistry, 65, 389–430.
- 531 Hong, J.X., Zhang, H.Y., Li, D.F., Ouyang, Y.P., Zhai, D.G., Liu, F., and Liu, J.J. (2022)
532 In situ LA-ICP-MS U-Pb geochronology and geochemical characteristics of
533 garnet from the Zhuxi skarn W-Cu deposit, South China. Ore Geology Reviews,
534 140, 104577.
- 535 Huang, L.C., and Jiang, S.Y. (2014) Highly fractionated S-type granites from the giant
536 Dahutang tungsten deposit in Jiangnan orogen, Southeast China: Geochronology,
537 petrogenesis and their relationship with W-mineralization. Lithos, 202–203, 207–
538 226.
- 539 Kwak, T.A.P. (1987) W-Sn skarn deposits and related metamorphic skarns and
540 granitoids. Developments in Economic Geology, 24, 1–450.
- 541 Li, X.H. (1999) U-Pb zircon ages of granites from the southern margin of the Yangtze
542 block: Timing of Neoproterozoic Jinning orogeny in SE China and implications
543 for Rodinia assembly. Precambrian Research, 97, 43–57.
- 544 Li, X.H., and Mcculloch, M.T. (1996) Secular variation in the Nd isotopic composition
545 of Neoproterozoic sediments from the southern margin of the Yangtze Block:
546 evidence for a Proterozoic continental collision in southeast China. Precambrian
547 Research, 76, 67–76.
- 548 Li, Y., Yuan, Y., Jowitt, S.M., Li, X.L., Zhou, T.F., Wang, F.Y., and Deng, Y.F. (2022)
549 Combined garnet, scheelite and apatite U-Pb dating of mineralizing events in the
550 Qiaomaishan Cu-W skarn deposit, eastern China. Geoscience Frontiers, 101459.
- 551 Linnen, R.L., and Williams-Jones, A.E. (1995) Genesis of a magmatic metamorphic
552 hydrothermal system; the Sn-W polymetallic deposits at Pilok, Thailand.
553 Economic Geology, 90, 1148–1166.
- 554 Liu, B., Wu, Q.H., Li, H., Evans, N.J., Wu, J.H., Cao, J.Y., and Jiang, J.B. (2019)
555 Fault-fluid evolution in the Xitian W–Sn ore field (South China): Constraints from
556 scheelite texture and composition. Ore Geology Reviews, 114, 103140.

- 557 Liu, M., Song, S.W., Cui, Y.R., Chen, G.H., Rao, J.F., and Ouyang, Y.P. (2021) In-situ
558 U-Pb geochronology and trace element analysis for the scheelite and apatite from
559 the deep seated stratiform-like W (Cu) ore of the Zhuxi tungsten deposit,
560 northeastern Jiangxi Province. *Acta Petrologica Sinica*, 37, 717–732 (in Chinese
561 with English abstract).
- 562 Liu, S.B., Liu, Z.Q., Wang, C.H., Wang, D.H., Zhao, Z., and Hu, Z.H. (2017)
563 Geochemical characteristics of REEs and trace elements and Sm-Nd dating of
564 scheelite from the Zhuxi giant tungsten deposit in northeast Jiangxi. *Earth Science
565 Frontiers*, 24, 17–30 (in Chinese with English abstract).
- 566 Liu, Y.S., Gao, S., Hu, Z.C., Gao, C.G., Zong, K.Q., and Wang, D.B. (2010)
567 Continental and oceanic crust recycling-induced melt-peridotite interactions in the
568 Trans-North China Orogen: U-Pb dating, Hf isotopes and trace elements in zircons
569 of mantle xenoliths. *Journal of Petrology*, 51, 537–571.
- 570 Liu, Z.Q., Liu, S.B., Chen, Y.C., Wang, C.H., Wan, H.Z., Chen, G.H., Li, S.S., and
571 Liang, L.J. (2014) LA-ICP-MS Zircon U-Pb Isotopic Dating of Lamprophyre
572 Located Zhuxi Copper-Tungsten Mine of Jiangxi Province and Its Geological
573 Significance. *Rock and Mineral Analysis*, 2014, 35, 758–766 (in Chinese with
574 English abstract).
- 575 Ludwig, K.R. (2012) User's manual for Isoplot/Ex rev. 3.75-4.15: A geochronological
576 toolkit for Microsoft Excel. Berkeley Geochronology Center Special Publication.
- 577 Mao, J.W., Xiong, B.K., Liu, J., Pirajno, F., Cheng, Y.B., Ye, H.S., Song, S.W., and Dai,
578 P. (2017) Molybdenite Re-Os dating, zircon U-Pb age and geochemistry of
579 granitoids in the Yangchuling porphyry W-Mo deposit (Jiangnan tungsten ore
580 belt), China: Implications for petrogenesis, mineralization and geodynamic setting.
581 *Lithos*, 286–287, 35–52.
- 582 Mao, J.W., Wu, S.H., Song, S.W., Dai, P., Xie, G.Q., Su, Q.W., Liu, P., Wang, X.G., Yu,
583 Z.Z., Chen, X.Y., and Tang, W.X. (2020) The world-class Jiangnan tungsten belt:
584 Geological characteristics, metallogeny, and ore deposit model. *Chinese Science*

- 585 Bulletin, 65, 3746–3762 (in Chinese with English abstract).
- 586 Mao, Z.H., Liu, J.J., Mao, J.W., Deng, J., Zhang, F., Meng, X.Y., Xiong, B.K., Xiang,
587 X.K., and Luo, X.H. (2015) Geochronology and geochemistry of granitoids
588 related to the giant Dahutang tungsten deposit, Middle Yangtze River region,
589 China: Implications for petrogenesis, geodynamic setting, and mineralization.
590 Gondwana Research, 28, 816–836.
- 591 Meinert, L.D., Dipple, G.M., and Nicolescu, S. (2005) World skarn deposits. Economic
592 Geology, 98, 147–156.
- 593 Nassau, K., and Loiacono, G. (1963) Calcium tungstate—III: Trivalent rare earth
594 substitution. Journal of Physics and Chemistry of Solids, 24, 1503–1510.
- 595 Nguyen, T. H., Nevolko, P. A., Pham, T. D., Svetlitskaya, T. V., Tran, T. H., Shelepaev,
596 R. A., Fominykh, F.A., and Pham, N. C. (2020) Age and genesis of the W-Bi-Cu-F
597 (Au) Nui Phao deposit, Northeast Vietnam: Constrains from U-Pb and Ar-Ar
598 geochronology, fluid inclusions study, S-O isotope systematic and scheelite
599 geochemistry. Ore Geology Reviews, 123, 103578.
- 600 No. 912 Geological Team, Bureau of Geology and Mineral Resources of Jiangxi
601 Province (No. 912 Geological Team). (2020) Final Report to General Survey of
602 Zhuxi Tungsten and Copper Metallogenic Deposit in Fuliang County, Jiangxi
603 Province. pp. 158–186 (in Chinese).
- 604 Ouyang, Y.P., Zhou, X.R., Yao, Z.Y., Rao, J.F., Song, S.W., Wei, J., and Lu, Y. (2020)
605 Study on the two-stage garnets and their indication of mineralization in the Zhuxi
606 W (Cu) deposit, northeastern Jiangxi Province. Earth Science Frontiers, 27, 219–
607 231 (in Chinese with English abstract).
- 608 Pan, X.F., Hou, Z.Q., Li, Y., Chen, G.H., Zhao, M., Zhang, T.F., Zhang, C., Wei, J., and
609 Kang, C. (2017) Dating the giant Zhuxi W(Cu) deposit (Taqian-Fuchun Ore Belt)
610 in South China using molybdenite Re-Os and muscovite Ar-Ar system. Ore
611 Geology Reviews, 86, 719–733.
- 612 Pan, X.F., Hou, Z.Q., Zhao, M., Chen, G.H., Rao, J.F., Li, Y., Wei, J., and Ouyang, Y.P.

- 613 (2018) Geochronology and geochemistry of the granites from the Zhuxi W(Cu)ore
614 deposit in South China: Implication for petrogenesis, geodynamical setting and
615 mineralization. *Lithos*, 304–307, 155–179.
- 616 Poulin, R.S., Kontak, D.J., McDonald, A.M., and McClenaghan, M.B. (2018)
617 Assessing scheelite as an ore-deposit discriminator using its trace-element and
618 REE chemistry. *Canadian Mineralogist*, 56, 265–302.
- 619 Poitrenaud, T., Poujol, M., R Augier, and Marcoux, E. (2020) The polyphase evolution
620 of a late Variscan W/Au deposit (Aalau, French Pyrenees): Insights from REE and
621 U/Pb LA-ICP-MS analyses. *Mineralium Deposita*, 55, 1127–1147.
- 622 Romer, R.L., Heinrich, W., Schröder-Smeibidl, B., Meixner, A., Fischer, C.O., and
623 Schulz, C. (2005) Elemental dispersion and stable isotope fractionation during
624 reactive fluid flow and fluid immiscibility in the Bufa del Diente aureole,
625 NE-Mexico: Evidence from radiographies and Li, B, Sr, Nd, and Pb isotope
626 systematics. *Contributions to Mineralogy and Petrology*, 149, 400–429.
- 627 Sciuba, M., Beaudoin, G., Grzela, D., and Makvandi, S. (2020) Trace element
628 composition of scheelite in orogenic gold deposits. *Mineralium Deposita*, 55,
629 1149–1172.
- 630 Song, G.X., Qin, K.Z., Li, G.M., Liu, T.B., Li, J.X., Li, X.H., and Chang, Z.S. (2012)
631 Geochronologic and isotope geochemical constraints on magmatism and
632 associated W-Mo mineralization of the Jitoushan W-Mo deposit, Middle-Lower
633 Yangtze Valley. *International Geology Review*, 54, 1532–1547.
- 634 Song, G.X., Qin, K.Z., Li, G.M., Evans, N.J., and Chen, L. (2014) Scheelite elemental
635 and isotopic signatures: Implications for the genesis of skarn-type W-Mo deposits
636 in the Chizhou Area, Anhui Province, Eastern China. *American Mineralogist*, 99,
637 303–317.
- 638 Song, S.W., Mao, J.W., Xie, G.Q., Chen, L., Santosh, M., Chen, G.H., Rao, J.F., and
639 Ouyang, Y.P. (2019) In situ LA-ICP-MS U-Pb geochronology and trace element
640 analysis of hydrothermal titanite from the giant Zhuxi W(Cu) skarn deposit, South

- 641 China. *Mineralium Deposita*, 54, 569–590.
- 642 Song, S.W., Mao, J.W., Xie, G.Q., Yao, Z.Y., Chen, G.H., Rao, J.F., and Ouyang, Y.P.
643 (2021) Petrogenesis of Scheelite-Bearing Albitite as an Indicator for the
644 Formation of a World-Class Scheelite Skarn Deposit: A Case Study of the Zhuxi
645 Tungsten Deposit. *Economic Geology*, 116, 91–121.
- 646 Su, Q.W., Mao, J.W., Wu, S.H., Zhang, Z.C., and Xu, S.F. (2018) Geochronology and
647 geochemistry of the granitoids and ore-forming age in the Xiaoyao tungsten
648 polymetallic skarn deposit in the Jiangnan Massif tungsten belt, China:
649 Implications for their petrogenesis, geodynamic setting, and mineralization.
650 *Lithos*, 296–299, 365–381.
- 651 Su, S.Q., Qin, K.Z., Li, G.M., Large, R.R., Olin, P., and Evans, N.J. (2021) Constraints
652 on scheelite genesis at the Dabaoshan stratabound polymetallic deposit, South
653 China. *American Mineralogist*, 106, 1503–1519.
- 654 Sun, K.K., and Chen, B. (2017) Trace elements and Sr-Nd isotopes of scheelite:
655 Implications for the W-Cu-Mo polymetallic mineralization of the Shimensi
656 deposit, South China. *American Mineralogist*, 102, 1114–1128.
- 657 Sun, K.K., Chen, B., and Deng, J. (2019) Ore genesis of the Zhuxi supergiant W-Cu
658 skarn polymetallic deposit, South China: Evidence from scheelite geochemistry.
659 *Ore Geology Reviews*, 107, 14–29.
- 660 Sun, S.S., and McDonough, W.F. (1989) Chemical and isotopic systematics of oceanic
661 basalts: Implications for mantle composition and processes. *Geological Society*
662 *London Special Publications*, 42, 313–345.
- 663 Thomas, R., Förster, H.J., Rickers, K., and Webster, J.D. (2005) Formation of
664 extremely F-rich hydrous melt fractions and hydrothermal fluids during
665 differentiation of highly evolved tin-granite magmas: A melt/fluid-inclusion study.
666 *Contributions to Mineralogy and Petrology*, 148, 582–601.
- 667 Wang, X.L., Zhou, J.C., Griffin, W.L., Wang, R.C., Qiu, J.S., O'Reilly, S.Y., Xu, X.S.,
668 Liu, X.M., and Zhang, G.L. (2007) Detrital zircon geochronology of Precambrian

- 669 basement sequences in the Jiangnan orogen: Dating the assembly of the Yangtze
670 and Cathaysia blocks. *Precambrian Research*, 159, 117–131.
- 671 Wang, X.L., Zhou, J.C., Griffin, W.L., Zhao, G.C., Yu, J.H., Qiu, J.S., Zhang, Y.J., and
672 Xing, G.F. (2014) Geochemical zonation across a Neoproterozoic orogenic belt:
673 Isotopic evidence from granitoids and metasedimentary rocks of the Jiangnan
674 orogen, China. *Precambrian Research*. 242, 154–171.
- 675 Webster, J., Thomas, R., Förster, H.J., Seltmann, R., and Tappen, C. (2004)
676 Geochemical evolution of halogen-enriched granite magmas and mineralizing
677 fluids of the Zinnwald tin-tungsten mining district Erzgebirge, Germany.
678 *Mineralium Deposita*, 39, 452–472.
- 679 Wintzer, N.E., Gillerman, V.S., and Schmitz, M.D. (2016) Eocene U/Pb scheelite
680 LA-ICP-MS dates of stibnite-scheelite mineralization in the Yellow Pine
681 Au-Sb-W mining area, Central Idaho, USA. GSA annual meeting, Denver.
- 682 Wu, F.Y., Yang, Y.H., Xie, L.W., Yang, J.H., and Xu, P. (2006) Hf isotopic compositions
683 of the standard zircons and baddeleyites used in U-Pb geochronology. *Chemical
684 Geology*, 234, 105–126.
- 685 Xu, J., Ciobanu, C.L., Cook, N.J., Zheng, Y.Y., Sun, X., and Wade, B.P. (2016) Skarn
686 formation and trace elements in garnet and associated minerals from Zhibula
687 copper deposit, Gangdese Belt, southern Tibet. *Lithos*, 262, 213–231.
- 688 Xu, R., Romer, R.L., and Glodny, J. (2022) Metal mobilization and precipitation in a
689 Sn-W skarn system, Gejiu Sn district, China. *Lithos*, 414–415, 106621.
- 690 Yardley, B.W.D., and Lloyd, G.E. (1995) Why metasomatic fronts are really
691 metasomatic sides. *Geology*, 23, 53–56.
- 692 Yuan, L.L., Chi, G.X., Wang, M.Q., Li, Z.H., Xu, D.R., Deng, T., Geng, J.Z., Hu, M.Y.,
693 and Zhang, L. (2019) Characteristics of REEs and trace elements in scheelite from
694 the Zhuxi W deposit, South China: Implications for the ore-forming conditions
695 and processes. *Ore Geology Review*, 109, 585–597.
- 696 Yuan, S.D., Peng, J.T., Hu, R.Z., Li, H.M., Shen, N.P., and Zhang, D.L. (2008) A

- 697 precise U–Pb age on cassiterite from the Xianghualing tin–polymetallic deposit
698 (Hunan, South China). *Mineralium Deposita*, 43, 375–382.
- 699 Zhang, Y.J., Liao, X.B., Zhou, X.H., Jiang, Y., Yu, M.G., Jiang, R., Zhao, X.L., Chen,
700 Z.H., Zhao, L., and Huang, W.C. (2012) Element characteristics and prominence
701 analysis of meta-argillo-arenaceous rocks in Zhanggongshan area, Anhui-Jiangxi
702 border region. *Geology in China*, 39, 1183–1198 (in Chinese with English
703 abstract).
- 704 Zhang, W., Jiang, S.Y., Gao, T.S., Ouyang, Y.P., and Zhang, D. (2020) The effect of
705 magma differentiation and degassing on ore metal enrichment during the
706 formation of the world-class Zhuxi W-Cu skarn deposit: Evidence from U-Pb ages,
707 Hf isotopes and trace elements of zircon, and whole-rock geochemistry. *Ore
708 Geology Reviews*, 127, 103801.
- 709 Zhang, W., Jiang, S.Y., Ouyang, Y.P., and Zhang, D. (2021) Geochronology and
710 textural and compositional complexity of apatite from the mineralization-related
711 granites in the world-class Zhuxi W-Cu skarn deposit: A record of magma
712 evolution and W enrichment in the magmatic system. *Ore Geology Reviews*, 128,
713 103885.
- 714 Zhao, J.H., Zhou, M.F., Yan, D.P., Zheng, J.P., and Li, J.W. (2011) Reappraisal of the
715 ages of Neoproterozoic strata in South China: no connection with the Grenvillian
716 orogeny. *Geology*, 39, 299–302.
- 717 Zhao, W.W., Zhou, M.F., Li, Y.H.M., Zhao, Z., and Gao, J.F. (2017) Genetic types,
718 mineralization styles, and geodynamic settings of Mesozoic tungsten deposits in
719 South China. *Journal of Asian Earth Sciences*, 137, 109–140.
- 720 Zhao, W.W., Zhou, M.F., Williams-jones, A.E., and Zhao, Z. (2018) Constraints on the
721 uptake of REE by scheelite in the Baoshan tungsten skarn deposit. South China.
722 *Chemical Geology*, 477, 123–136.
- 723 Zhou, X., Yu, X.Q., Wang D.E., Zhang D.H., Li, C.L., and Fu, J.Z. (2011)
724 Characteristics and geochronology of the W, Mo-bearing granodiorite porphyry in

725 Dongyuan, southern Anhui. *Geoscience*, 25, 201–210 (in Chinese with English
726 abstract).

727 Zhu, D.P., Li, H., Algeo, T.J., Jiang, W.C., and Wang, C. (2021) The
728 prograde-to-retrograde evolution of the Huangshaping skarn deposit (Nanling
729 Range, South China). *Mineralium Deposita*, 56, 1087–1110.

730

731 **Figure captions**

732 Fig. 1 (a) A schematic map of the South China Craton (modified from [Mao et al.](#)
733 [2017](#)); (b) A tectonic map of South China showing the position of the Jiangnan
734 Orogenic Belt (modified from [Hong et al. 2022](#)); (c) A regional geological map of the
735 Jiangnan porphyry-skarn tungsten belt (JNB) showing the distributions of major W
736 deposits (modified from [Mao et al. 2017](#) and [Song et al. 2021](#)).

737

738 Fig. 2 (a) A geological map of the Zhuxi skarn deposit (modified from [Yuan et al.](#)
739 [2019](#)); (b-c) Representative cross-sections showing the local intrusions and W-Cu
740 orebodies (after [No. 912 Geological Team 2020](#)).

741

742 Fig. 3 Photographs of representative hand samples showing paragenetic sequences of
743 the Zhuxi deposit. (a) Disseminated tungsten mineralization; (b) Coarse-grained
744 scheelite coexisting with tremolite and minor chalcopyrite; (c) Disseminated scheelite
745 in marble cut by a scheelite-muscovite vein; (d) A vein of
746 garnet-pyroxene-wollastonite in marble, with minor scheelite; (e) Disseminated
747 scheelite in garnet skarn; (f) Scheelite cut by a quartz-sulfide vein. Insets (and panel f)
748 show long-wave UV images of the samples. Abbreviations: Ccp-chalcopyrite;
749 Grt-garnet; Mb-marble; Ms-muscovite; Pyx-pyroxene; Qz-quartz; Sch-scheelite;
750 Tr-tremolite; Wo-wollastonite.

751

752 Fig. 4 Photomicrographs of thin sections showing the mineral assemblages of the

753 Zhuxi deposit. (a) A garnet-pyroxene-wollastonite vein in prograde skarn stage; (b-c)
754 Garnet replaced by disseminated scheelite (Sch A); (d) Scheelite (Sch B) coexisting
755 with muscovite and quartz; (e) Disseminated scheelite (Sch B) in retrograde skarn
756 stage; (f) Coarse-grained scheelite (Sch C, up to 0.5 cm) in retrograde skarn stage; (g)
757 Sch B replaced by chalcopyrite; (h) Chalcopyrite intergrown with sphalerite,
758 bismuthinite, and native bismuth; (i) Sch B cut by a later calcite vein. All pictures are
759 performed under cross-polarized light, except for panels g and h, which are reflected
760 light. Abbreviations: Bi-native bismuth; Bmt-bismuthinite; Cal-calcite;
761 Ccp-chalcopyrite; Grt-garnet; Ms-muscovite; Qz-quartz; Sch-scheelite; Sph-sphalerite;
762 Wo-wollastonite.

763

764 Fig. 5 Representative cathodoluminescence (CL) images of scheelite from the Zhuxi
765 deposit. (a) Sch A with weak oscillatory zoning; (b) Sch B with notable oscillatory
766 zoning; (c-d) Coarse-grained Sch C showing a CL-dark core with oscillatory zoning.

767

768 Fig. 6 Chondrite-normalized REE patterns for different generations of scheelite from
769 the Zhuxi deposit. The normalized values for chondrite are from Sun and McDonough
770 (1989). Granite and garnet data are collected from Pan et al. (2018), Zhang et al.
771 (2020), and Hong et al. (2022).

772

773 Fig. 7 Binary plots of (a) Sr vs. Mo; (b) REE vs. Sr; (c) REE-Eu+Y (representing
774 REE³⁺) vs. Nb; (d) Mo vs. Nb for different generations of scheelite from the Zhuxi
775 deposit. Grey arrows schematically indicate that the Sr and REE contents increase from
776 Sch A to Sch C, while the Mo contents decrease.

777

778 Fig. 8 Tera-Wasserburg concordia diagrams of the corresponding ²⁰⁷Pb-corrected
779 ²⁰⁶Pb/²³⁸U ages for scheelites from the Zhuxi deposit. (a-b) U-Pb ages for
780 disseminated Sch A; (c-d) U-Pb ages for disseminated Sch B; (e-f) U-Pb ages for

781 coarse-grained massive Sch C. The uncertainties are quoted as 2σ .

782

783 Fig. 9 Discrimination diagrams for different generations of scheelite. (a) Plot of
784 chondrite-normalized Eu concentrations (Eu_N) vs. calculated Eu^*_N values, where Eu^*_N
785 $= (Sm_N \times Gd_N)^{1/2}$; (b) Plot of Eu_N/Eu^*_N (δEu) vs. Mo; (c) Plot of Eu_N/Eu^*_N (δEu) vs. Sr;
786 (d) Plot of Ce vs. Mo; (e) Plot of δCe vs. Mo; (f) Plot of δCe vs. δEu .

787

788 Fig. 10 (a) Plot of Y vs. Ho (after [Ding et al. 2018](#)); (b) Plot of Y/Ho vs. δEu . Data from
789 Pan et al. (2018), Sun et al. (2019), Yuan et al. (2019), Liu et al. (2021), Zhang et al.
790 (2020), Zhang et al. (2021) and Hong et al. (2022). Insets in b show that the core of
791 the Sch C with dark CL image has relatively high Y/Ho and δEu values.

792

793 Table 1. Major element results of scheelite from the Zhuxi W deposit (wt.%)

794

795 Table 2. Summarized LA-ICP-MS trace element results of scheelite from the Zhuxi W
796 deposit (ppm)

797

798 Appendix Figure A1. Representative time-resolved depth profiles of scheelite showing
799 smooth curves for all the selected elements.

800

801 Appendix Table A1. LA-ICP-MS trace element results of scheelite from the Zhuxi W
802 deposit (ppm)

803

804 Appendix Table A2. LA-ICP-MS U-Pb dating results for scheelite from the Zhuxi
805 deposit

806

Table 1. Major elements results of scheelite from the Zhuxi W deposit (wt.%)

Spot No.	MoO ₃	Na ₂ O	TiO ₂	MnO	CaO	FeO	Nb ₂ O ₅	Ta ₂ O ₅	UO ₃	WO ₃	Total
18zx-13q1d1	0.02	bd	bd	bd	19.86	0.01	bd	bd	0.03	79.89	99.81
18zx-14q1d1	0.18	bd	0.01	bd	19.72	bd	0.06	bd	bd	79.11	99.07
18zx-17q1d1	0.01	bd	0.01	bd	18.50	0.01	bd	bd	0.04	78.52	97.09
18zx-18q1d1	bd	bd	0.01	bd	19.56	0.03	bd	bd	0.01	80.41	100.01
18zx-21q1d1	0.05	bd	0.03	bd	18.45	0.03	bd	bd	0.01	80.86	99.43
18zx-21q1d2	0.04	0.01	bd	0.02	20.08	bd	bd	bd	bd	80.55	100.68

Note: bd= below detection.

Table 2. Summarized LA-ICP-MS trace element results of scheelite from the Zhuxi W deposit (ppm)

Sample No.	Sr	Nb	Mo	La	Ce	Pr	Nd	Sm	Eu	Gd	Tb	Dy	Ho	Er	Tm	Yb	Lu	Hf	Ta	Y	ΣREE	δEu	δCe	Y/Ho	
Sch A (n=20)																									
Mean	10	87	1002	1.2	1.3	0.09	0.25	0.06	0.05	0.04	0.01	0.06	0.01	0.03	0.005	0.03	0.004	0.014	1	0.4	3.2	9.6	0.8	74	
S.D.	2	70	293	1	1.7	0.08	0.28	0.09	0.03	0.06	0.01	0.08	0.01	0.04	0.005	0.03	0.006	0.036	0.8	0.4	2.7	12	0.1	43	
Min	8	23	557	0.1	0.1	0.01	0.01	0.01	0.02	0.01	0.001	0.002	0.0003	0.001	0.001	0.01	0.001	0.001	0.2	0.04	0.3	0.9	0.5	31	
Max	16	274	1680	3.3	7.5	0.32	1.13	0.35	0.11	0.24	0.05	0.3	0.05	0.14	0.02	0.13	0.02	0.156	3.3	1.6	11	54	1.2	207	
Sch B (n=20)																									
Mean	39	23	109	22	30	2.9	8.4	2.3	6.4	2.4	0.5	3.8	0.7	2.7	0.6	6.7	1.1	0.004	1.6	56.2	90	18.4	0.9	86	
S.D.	6	15	22	13	17	1.7	6	2	4.4	2.2	0.4	2.9	0.5	1.8	0.4	4.7	0.7	0.002	1.5	43	47	19	0.04	39	
Min	20	12	69	7.4	6.9	0.5	1.1	0.2	0.8	0.24	0.05	0.4	0.1	0.3	0.1	1.3	0.2	0.002	0.6	9	22	1.3	0.8	39	
Max	45	80	167	61	78	7.3	25.7	7.9	16.9	8.2	1.7	11	1.9	5.8	2	23	3.7	0.008	7	187	215	65	1	190	
Sch C (n=20)																									
Mean	58	135	45	73	131	15.5	52	14.6	7	13.4	2.8	19	3.5	11.2	2.1	17.6	2.5	0.004	8.3	151	364	7	1	72	
S.D.	10	204	13	52	103	16	65	21	4	20	4	25	4.4	12	1.7	12	1.7	0.002	14	116	313	9	0.1	49	
Min	42.4	10	25.5	6.3	19.9	2	4.3	0.9	1.4	0.6	0.2	1.5	0.3	1.2	0.3	2.4	0.3	0.001	0.4	21.3	50	0.4	1	27	
Max	72	619	74.7	152	334	51	212	68	13.1	66.3	13.1	83	14.5	40	5.7	34	5.3	0.01	41	403	1064	36.2	1.3	213	

Note: S.D. = standard deviation values.

Fig. 1

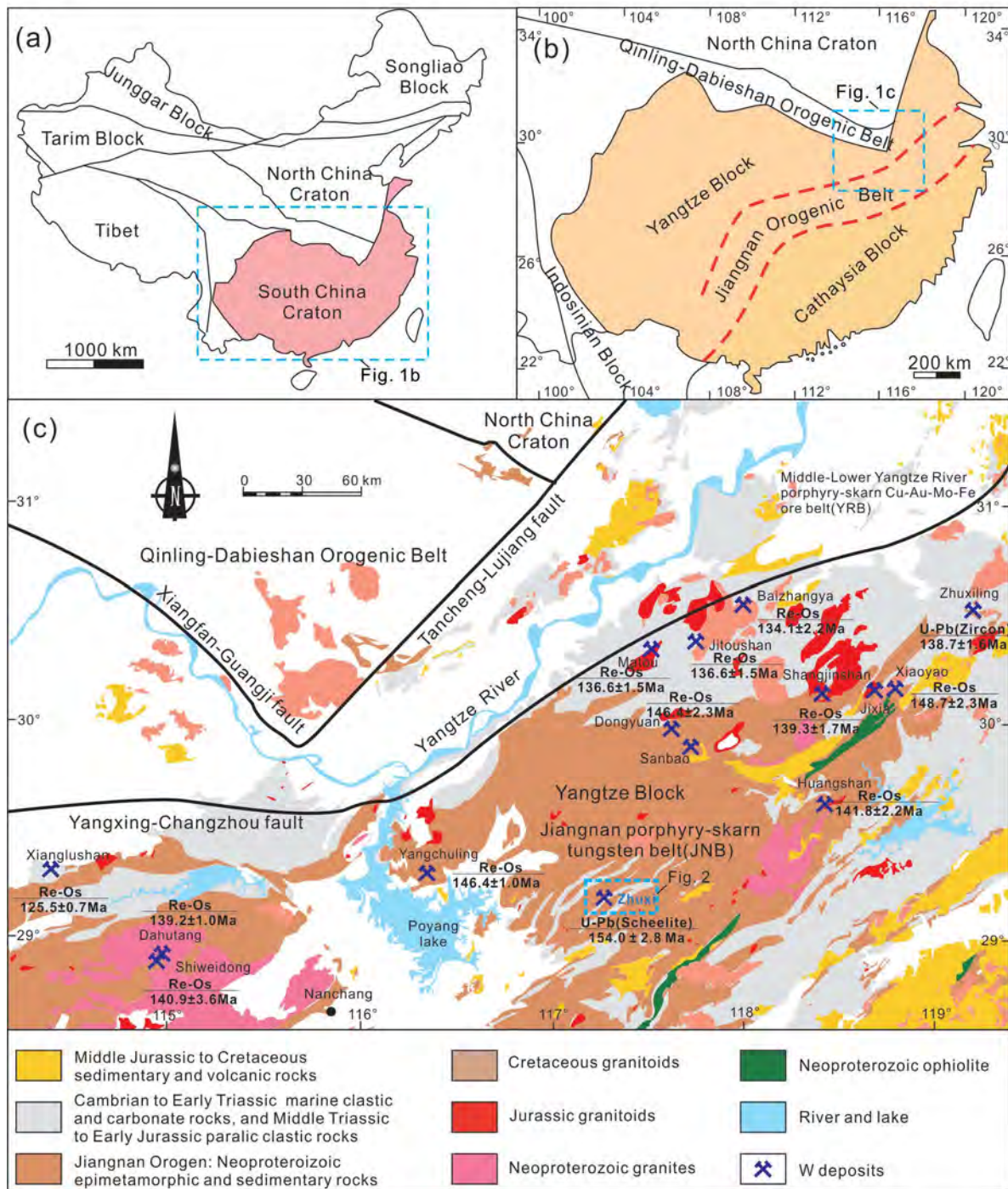


Fig. 2

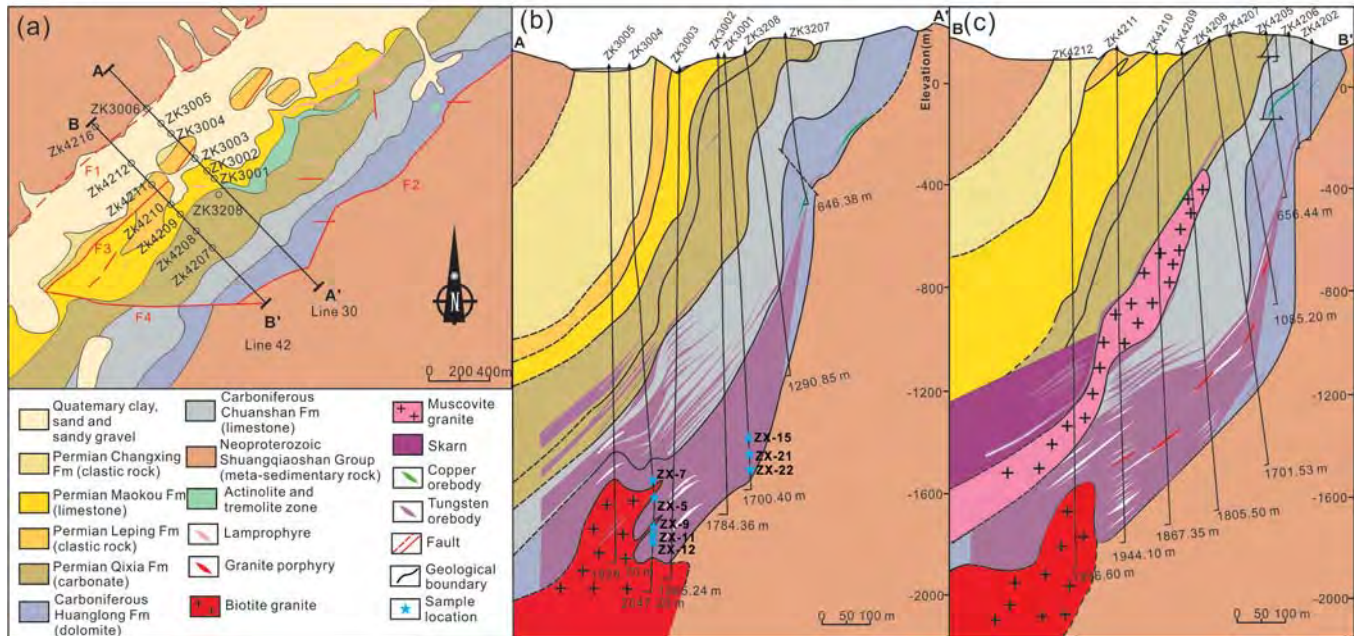


Fig. 3

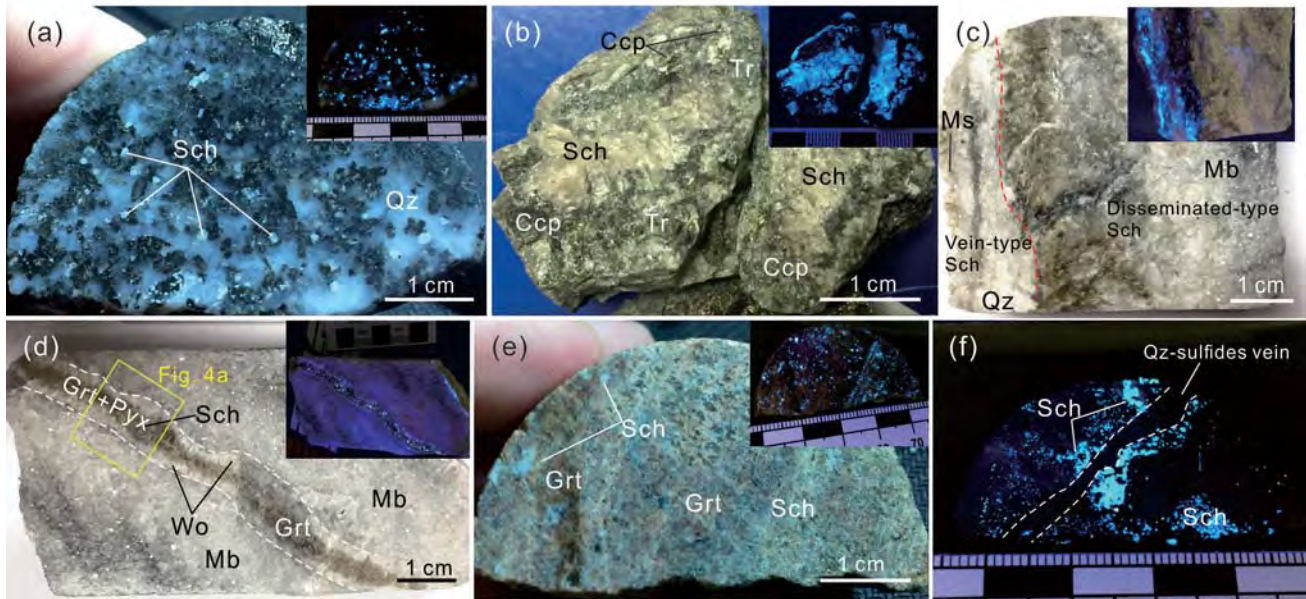


Fig. 4

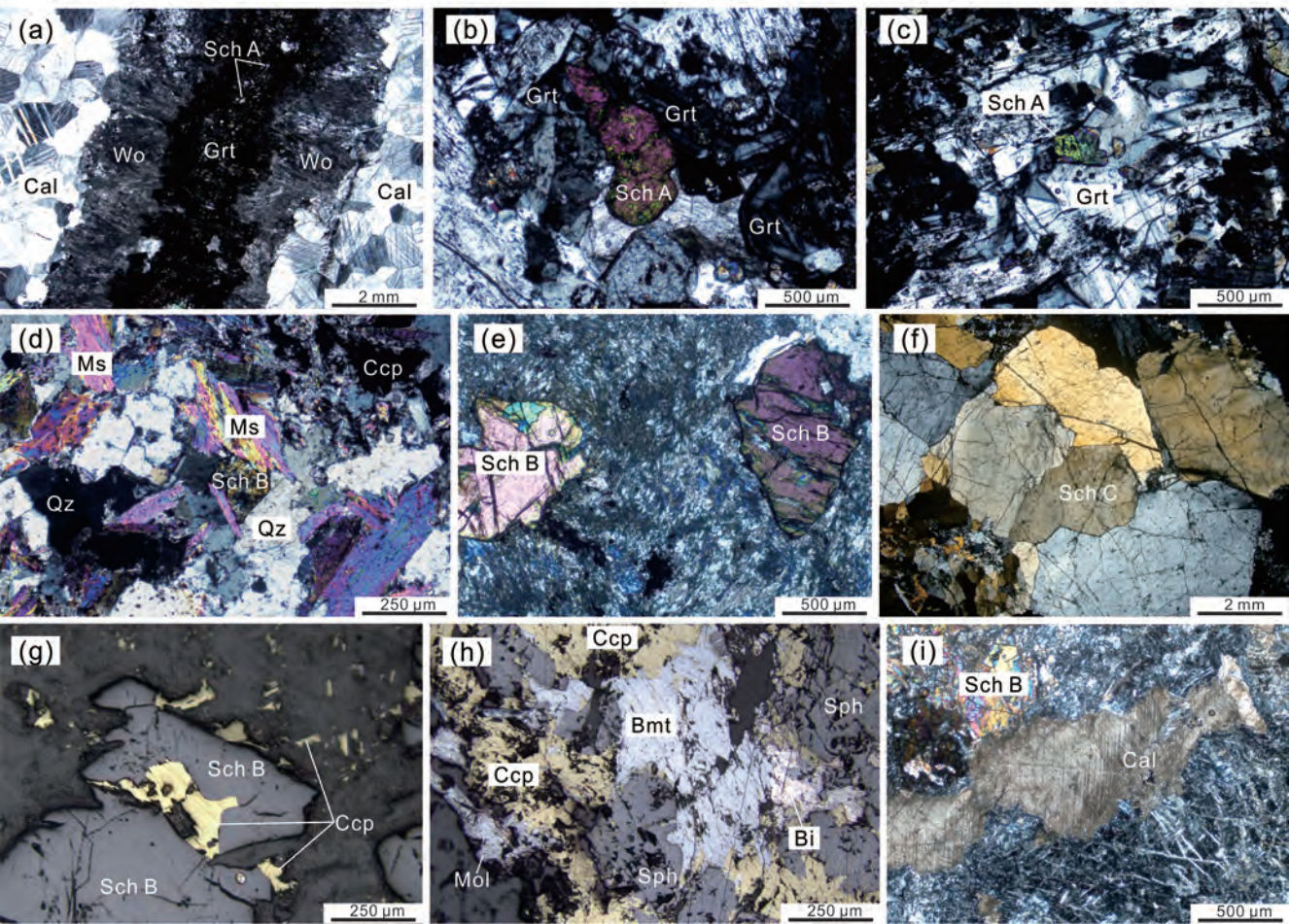


Fig. 5

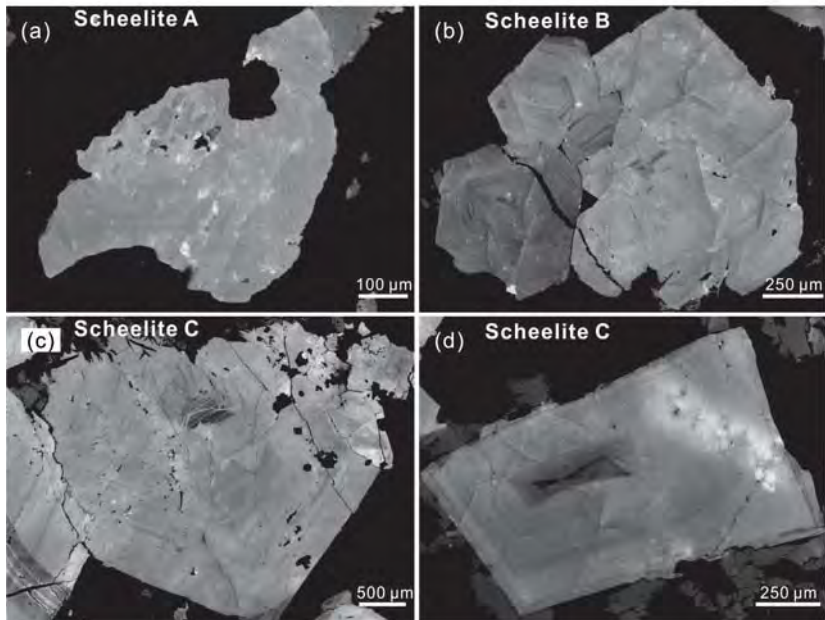


Fig. 6

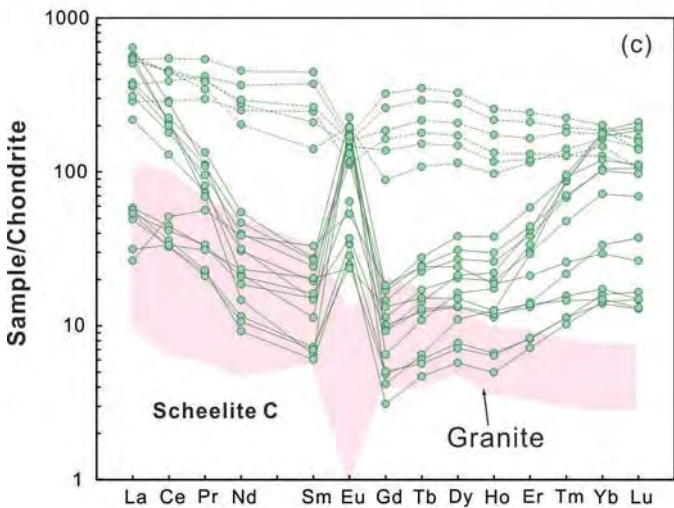
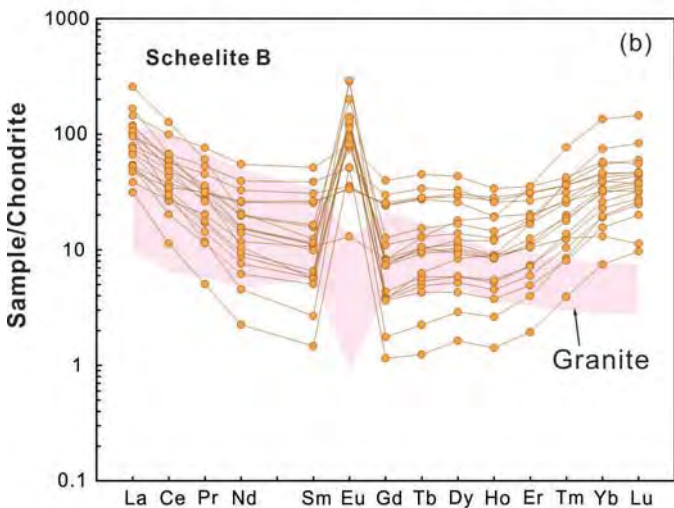
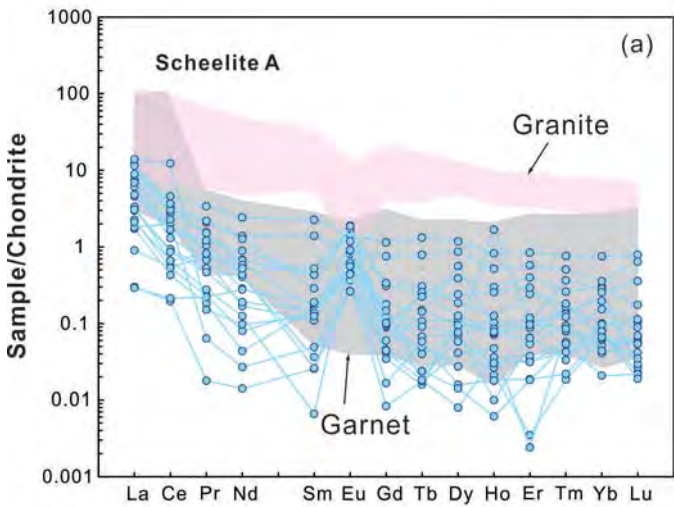


Fig. 7

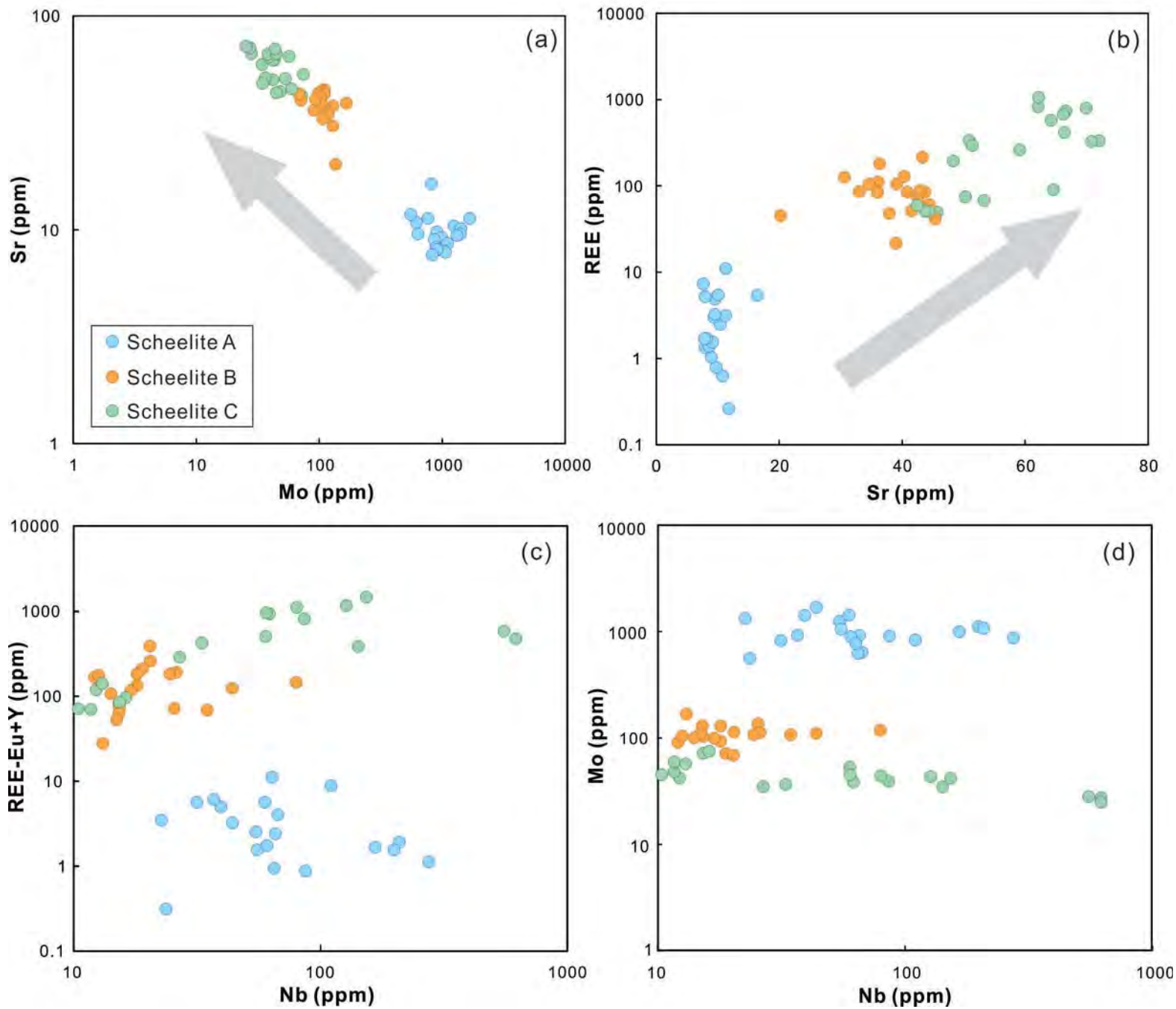


Fig. 8

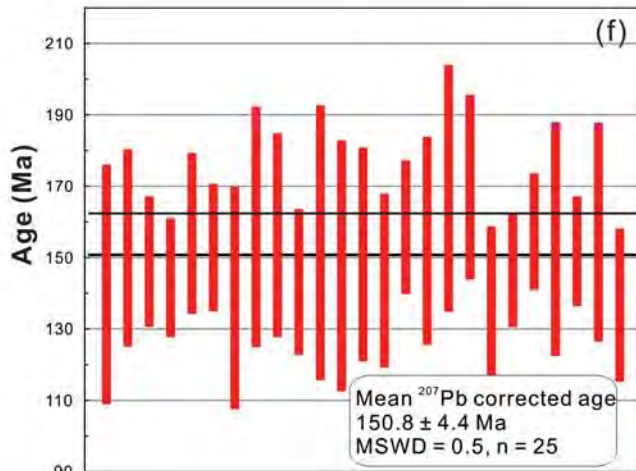
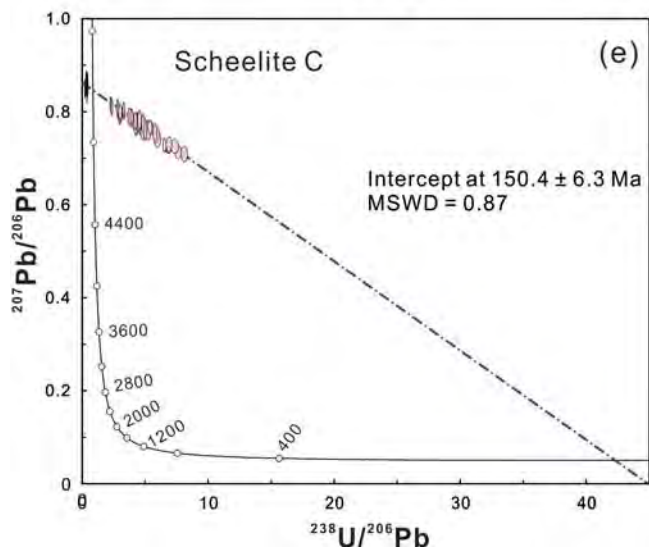
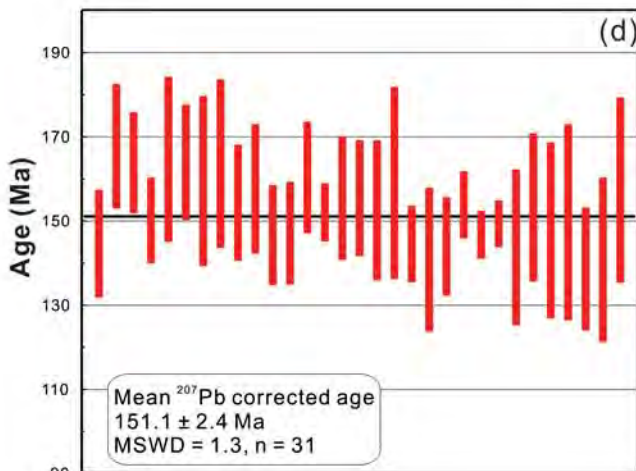
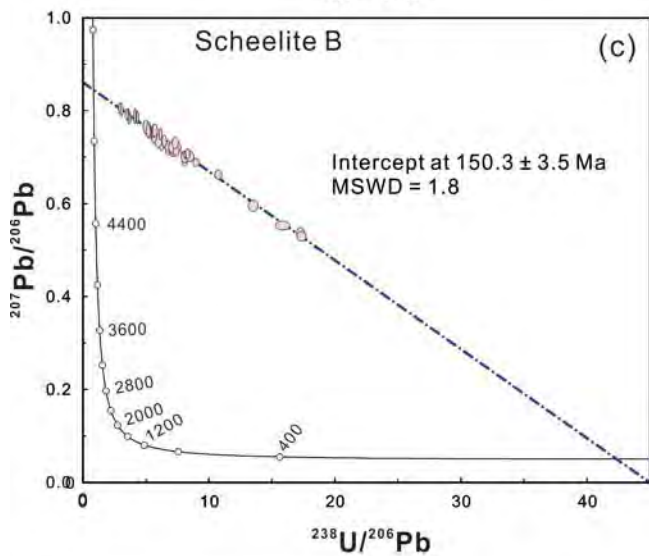
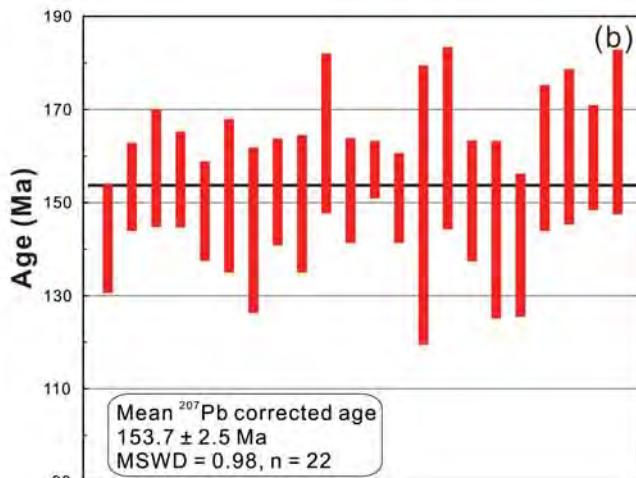
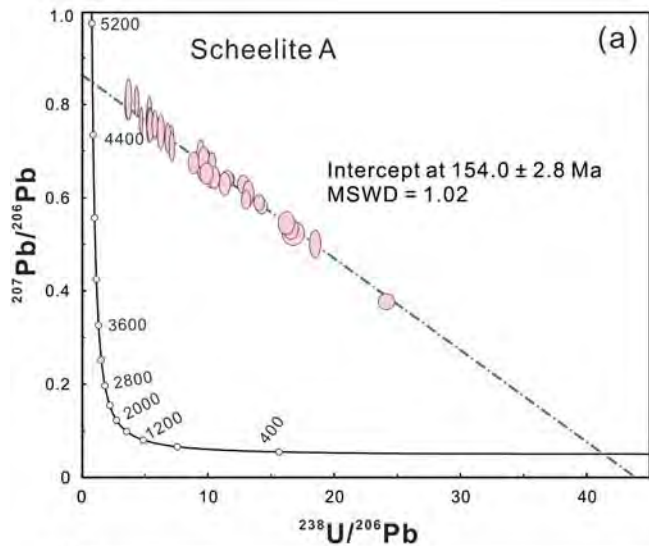


Fig. 9

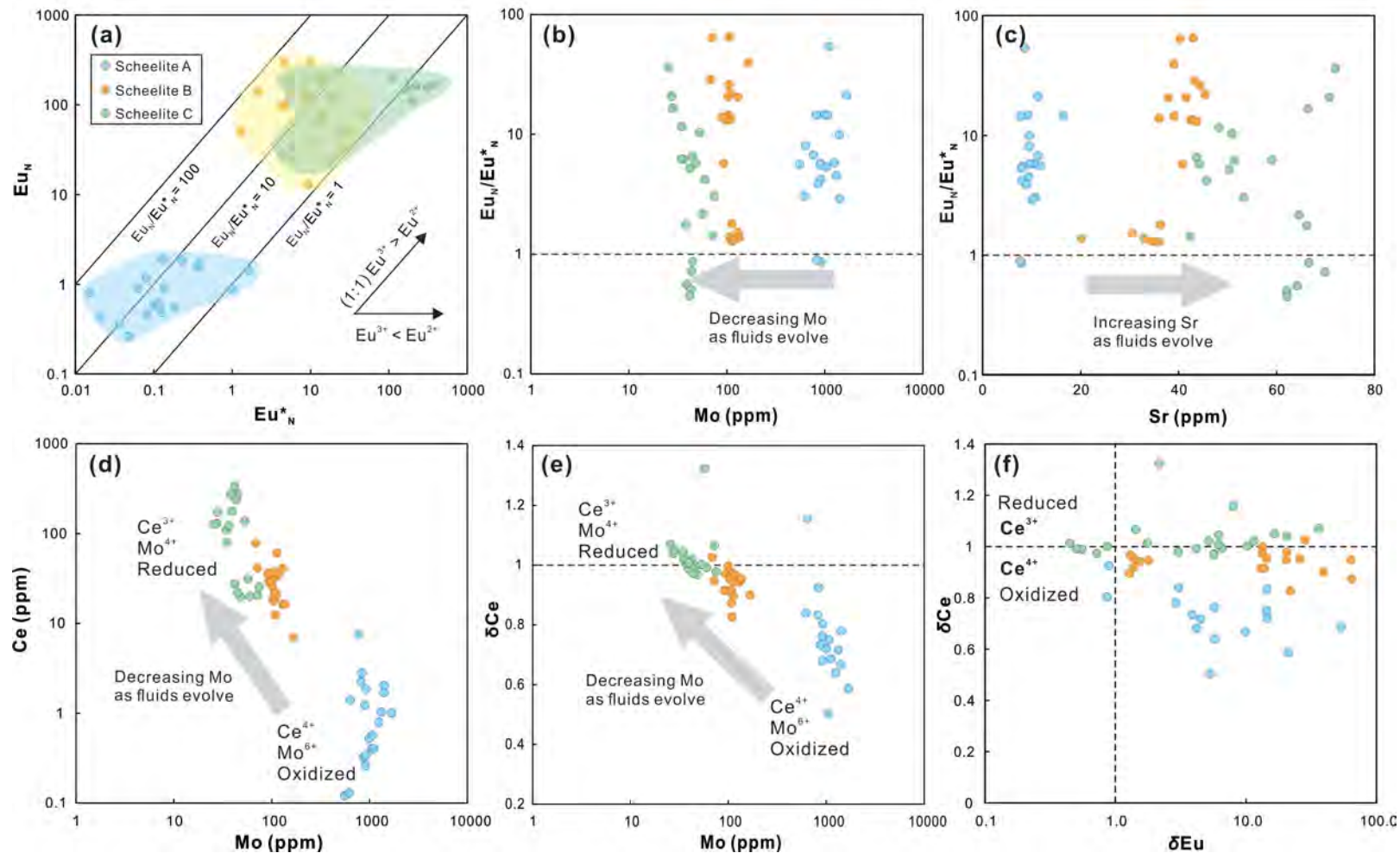


Fig. 10

